A motion estimation and compensation algorithm for 4D CBCT with cyclic deformation model

Alexander Katsevich, Seongjin Yoon, Michael Frenkel, Peter Munro, Pascal Paysan, Igor Peterlik, Dieter Seghers, and Adam Strzelecki

***Abstract*—We propose an algorithm for motion estimation and compensation in the case of a slowly rotating gantry in the 4D CBCT setting. Our primary target application is abdomen imaging, which is challenging because of the lack of high-contrast features. The algorithm is based on alternating application of volume estimation and motion estimation sub-iterations. The algorithm uses the optical flow constraint, and the motion is described by a global in time deformation function $\mu(s,\vec{x})$. This function constrains the motion to be cyclic and allows us to easily incorporate the motion phase into the regularization functional. For improved stability, volume sub-iterations use motion vector fields derived from the current estimate of μ instead of μ itself. Results of experiments with simulated and three clinical datasets of the TrueBeam™ treatment device demonstrate that the algorithm presented in this paper can reduce artifacts and improve image quality compared to 4D CBCT clinical reconstructions currently utilized for imaging of the abdomen.**

***Index Terms*—4D CBCT, motion estimation, motion compensation, optical flow constraint, dynamic regularization strength selection, abdomen imaging.**

I. Introduction

4D cone beam computed tomography (CBCT) [1] has long been used to evaluate the motion of thoracic anatomy in radiation oncology. However, 4D CBCT reconstructions can suffer from severe view aliasing artifacts as well as motion artifacts from residual motion within each of the phase bins. Many algorithms to eliminate artifacts in 4D CBCT have been proposed (see e.g., [2]–[8]).

However, these algorithms generally rely on the presence of high contrast anatomy such as found in the thorax to perform well. Therefore, these algorithms have performed inconsistently in the abdomen. Iterative reconstruction algorithms based on enforcing the optical flow constraint (OFC) appear to be most powerful and can potentially provide clinically acceptable 4D CBCT image quality in the abdomen.

We previously proposed a motion vector field (MVF)-based OFC algorithm and tested it on simulated and clinical data [9]. The novel idea was that we change parameters of the cost functional in a dynamic fashion during optimization to steer the algorithm towards a solution with required properties, e.g., with reduced sparse view streaks. The results were promising, but still contained some false motion. After analyzing these results, we concluded that false motion tends to form a progressive wave that is stronger close to the patient boundary, where voxels located close to each other in space have different motion phases.

In an effort to reduce false motion further, we develop an OFC-based method that incorporates a cyclic deformation model. The method enforces the motion to be cyclic throughout the entire breathing cycle and gives us explicit control over the spatial phase of the each voxel motion. We tested the algorithm on simulated and clinical datasets. The results show significantly reduced false motion and sparse-view streaks.

A. Katsevich, S. Yoon, and M. Frenkel are with iTomography Corp., Texas Medical Center Innovation Institute, 2450 Holcombe Blvd, Houston, TX 77021, USA (e-mail: alexander@iTomography.com, syoon@iTomography.com, michael@iTomography.com).

A. Katsevich is also with the University of Central Florida, Mathematics Department, Orlando, FL 32816, USA.

A. Katsevich is a shareholder and chief technology officer of iTomography Corporation and, as such, may benefit financially as a result of the outcomes of the work reported in this publication.

P. Munro, P. Paysan, I. Peterlik, D. Seghers, and A. Strzelecki are with Varian Medical Systems Imaging Laboratory, Taefernstrasse 7, 5405 Daettwil, Switzerland (e-mail: Peter.Munro@varian.com, Pascal.Paysan@varian.com, Igor.Peterlik@varian.com, Dieter.Seghers@varian.com, Adam.Strzelecki@varian.com).

II. Motion estimation and compensation based on the parameterized cyclic deformation model

Let s be the time (and also phase) variable, and $\vec{x}$ the 3D space variable. The dynamic object is represented by a volume function $f(s,\vec{x})$ and a deformation $\vec{\mu}(s,\vec{x})$ so that $f(s,\mu(s,\vec{x})) = f_0(\vec{x})$. Here, $f_0(\vec{x})$ is the attenuation coefficient at reference time/phase.

In our previous work [9], we studied the Lagrangian approach, where the OFC is expressed in terms of the MVF by taking the time derivative of $f(s,\vec{x})$:

$$\frac{\partial f(s,\vec{x})}{\partial s} + \nabla f(s,\vec{x}) \cdot \vec{v}(s,\vec{x}) = 0, \tag{1}$$

where $\vec{v}(s,\vec{x})$ is the velocity vector at $\vec{x}$ at time s. While this gave us a simpler reconstruction approach, it was not sufficiently robust to capture the correct motion due to the ill-posedness of the CBCT reconstruction problem.

Instead of the MVF-based approach, we reformulate the OFC using a parameterized deformation function. Suppose the reconstruction volume grid is given by

$$\vec{x}_{\mathbf{i}} = (h_1 i_1, h_2 i_2, h_3 i_3),\ \mathbf{i} = (i_1, i_2, i_3), \quad \text{for } 0 \leqslant i_q < N_q,\ q = 1,2,3. \tag{2}$$

For all $\vec{x}$, we have $f(s,\vec{x}) \approx \sum_{\mathbf{i}} f_{\mathbf{i}}(s)\varphi_h(\vec{x} - \vec{x}_{\mathbf{i}})$, where φ_h is the tri-linear interpolation kernel.

Let s_p, $0 \leqslant p < N_p$ be the time corresponding to the pth breathing phase bin. One way to incorporate the OFC is via the ℓ-2 norm penalty:

$$\Phi_{\mathrm{f}\mu}(\mathbf{f},\vec{\mu}) = \frac{1}{2}\sum_{\mathbf{i}}\sum_{p}\left| f(s_{p+1},\vec{\mu}(s_{p+1},\vec{x}_{\mathbf{i}})) - f(s_p,\vec{\mu}(s_p,\vec{x}_{\mathbf{i}}))\right|^2. \tag{3}$$

Advantages of and possibilities for improvement with the deformation-based approach are numerous:

1) We can enforce that each particle moves periodically along a line segment (or, along an elliptical path).
2) Such a description has fewer parameters to compute, which makes the overall motion estimation and compensation problem more stable.
3) Having easy access to the phase information (as part of the deformation function), we can reduce the progressive wave that causes false circular motion by using appropriate regularization, and leave only the stationary wave that is more physical.
4) An advantage of (3) over (1) is that it does not use the derivatives of f; hence, the requirements on the smoothness of f are relaxed. This may lead to improved spatial and temporal resolution of the method.

We choose the motion model as follows so that each voxel moves along a linear path:

$$\vec{\mu}(s,\vec{x}) = \vec{x} + \left[\cos\left(2\pi\frac{s-\bar{s}(\vec{x})}{\Delta S}\right) - \cos\left(2\pi\frac{\bar{s}(\vec{x})}{\Delta S}\right)\right]\vec{u}(\vec{x}), \quad (4)$$

where the amplitude $\vec{u}(\vec{x})$ and phase $\bar{s}(\vec{x})$ are expressed as follows:

$$\vec{u}(\vec{x}) = \sum_{\mathbf{j}} \vec{u}_{\mathbf{j}}\hat{\varphi}(\vec{x}-\vec{m}_{\mathbf{j}}), \quad (5)$$

$$\bar{s}(\vec{x}) = \sum_{\mathbf{k}} \bar{s}_{\mathbf{k}}\check{\varphi}(\vec{x}-\vec{n}_{\mathbf{k}}). \quad (6)$$

Note that neither the grids $\vec{x}_{\mathbf{i}}$, $\vec{m}_{\mathbf{j}}$, and $\vec{n}_{\mathbf{k}}$ nor the interpolation functions $\varphi(\cdot)$, $\hat{\varphi}(\cdot)$ and $\check{\varphi}(\cdot)$ have to be the same. In general, $\vec{u}$ is smooth, and $\bar{s}$ is even smoother. This reflects the hypothesis that the variability of the phase of the breathing motion throughout the patient is much smaller than the variability of its amplitude. Thus, we want to use a sparse grid with a smooth interpolation function for $\vec{u}$, and an even sparser grid and a smoother interpolation function for $\bar{s}$.

Let $\mathbf{f}$, $\mathbf{u}$, and $\bar{\mathbf{s}}$ denote phase volume, motion amplitude, and motion phase parameters unrolled into 1D vectors, respectively. Adding regularization terms for the volume parameters $\mathbf{f}$ and motion parameters $\mathbf{u}$ and $\bar{\mathbf{s}}$, the total functional is as follows:

$$\Phi(\mathbf{f},\mathbf{u},\bar{\mathbf{s}}) = \Phi_{\mathrm{L}}(\mathbf{f}) + \lambda\Phi_{\mathrm{f}\mu}(\mathbf{f},\mathbf{u},\bar{\mathbf{s}}) + \kappa_{\mathrm{f}}\Phi_{\mathrm{R_f}}(\mathbf{f},\delta) + \kappa_{\mathrm{u}}\Phi_{\mathrm{R_u}}(\mathbf{u}) + \kappa_s\Phi_{\mathrm{R_s}}(\bar{\mathbf{s}}), \quad (7)$$

where $\Phi_{\mathrm{L}}(\mathbf{f})$ is the data fidelity functional (as used in the penalized weighted least-squares approach), $\Phi_{\mathrm{f}\mu}(\mathbf{f},\mathbf{u},\bar{\mathbf{s}})$ is the OFC as described in (3), $\Phi_{\mathrm{R_f}}(\mathbf{f})$ is the volume regularizer, $\Phi_{\mathrm{R_u}}(\mathbf{u})$ is the motion amplitude regularizer, $\Phi_{\mathrm{R_s}}(\bar{\mathbf{s}})$ is the motion phase regularizer, and λ, κ_{f}, κ_{u}, and κ_s are regularization weights. The four functionals in (7) are defined as follows:

$$\Phi_{\mathrm{L}}(\mathbf{f}) := \frac{1}{2}(\mathbf{G}-\mathbf{A}\mathbf{f})^{\mathsf{T}}\mathbf{W}(\mathbf{G}-\mathbf{A}\mathbf{f}), \quad (8)$$

$$\Phi_{\mathrm{R_f}}(\mathbf{f}) := \sum_q\sum_{\mathbf{i}}\phi_{\mathrm{R}}([\mathbf{C}_q\mathbf{f}]_{\mathbf{i}},\ \delta), \quad (9)$$

$$\Phi_{\mathrm{R}_u}(\mathbf{u}) =: \frac{1}{2}\sum_q\sum_r\sum_{\mathbf{j}}\left([\mathbf{C}_r\mathbf{u}_q]_{\mathbf{j}}\right)^2, \quad (10)$$

$$\Phi_{\mathrm{R}_s}(\bar{\mathbf{s}}) =: \frac{1}{2}\sum_r\sum_{\mathbf{k}}([\mathbf{C}_r\bar{\mathbf{s}}]_{\mathbf{k}})^2, \quad (11)$$

where $\mathbf{G}$ is the entire set of measured data, $\mathbf{u}_q$ is the component of $\mathbf{u}$ along the qth axis, $\mathbf{A}$ is the system matrix, $\mathbf{W}$ is the weight matrix, $\mathbf{C}_q$ is the spatial finite difference matrix along the qth axis with clamped boundaries, $\mathrm{diag}\{\mathbf{t}\}$ is the diagonal matrix with the elements of vector $\mathbf{t}$ on the main diagonal, $[\mathbf{t}]_i$ is the ith element (scalar, vector, or matrix) along the first dimension of vector or matrix $\mathbf{t}$, $\phi_{\mathrm{R}}(t,\ \delta)$ is the hyperbolic potential regularizer defined as follows

$$\phi_{\mathrm{R}}(t,\ \delta) = \delta^2\left(\sqrt{1+(t/\delta)^2}-1\right). \quad (12)$$

In general, $\mathbf{W}$ is derived from the raw projection data to account for relative noise intensity. For now, we set $\mathbf{W}$ to be the identity matrix. The dimensions of $\mathbf{C}_q$ is determined by the vector to which it applies.

As in the previous work [9], we use an alternating direction minimization scheme to find the optimal phase volume and motion parameters by repeatedly applying two separate sub-iteration steps. To find the optimal solution at each sub-iteration step, we use an approximated Newton's method with a separable surrogate function.

III. Hybrid deformation-velocity approach

In the deformation-based OFC shown in (3), pairs of consecutive phase volumes are compared using a reference grid that is regular only in the reference phase. This grid is far from regular after deformation. Even though the OFC encourages incompressibility, the estimated volume usually shows some compressibility (whether it is real or not), and the data density at the expanding region becomes sparse, causing the OFC to be applied unevenly. Consequently, the OFC fails to regularize the expanding or compressing regions properly, resulting in speckle artifacts when the data are noisy and not perfectly matching.

To address this instability due to the data grid irregularity, we modify the OFC for volume sub-iterations so that the reference grid, where two consecutive phase volumes are compared, is regular:

$$\Phi_{\mathrm{f}\mu}(\mathbf{f},\mathbf{u},\bar{\mathbf{s}}) = \frac{1}{2}\sum_{\mathbf{i}}\sum_p\left|f(s_{p+1},\vec{x}_{\mathbf{i}}+\vec{V}_p(\vec{x}_{\mathbf{i}})) - f(s_p,\vec{x}_{\mathbf{i}})\right|^2. \quad (13)$$

Here $\vec{V}_p(\vec{x}_{\mathbf{i}})$ is the estimated MVF field between pairs of consecutive phase volumes on a regular grid. Given $\vec{\mu}(s_p,\vec{x}_{\mathbf{i}})$, we compute the MVF $\vec{V}_p(\vec{x}_{\mathbf{i}})$ in a form analogous to (5), (6) with another grid $\vec{x}_{\mathbf{i}'}$ by solving the following optimization problem:

$$\vec{V}_p = \arg\min_{\vec{v}} \frac{1}{2}\sum_{\mathbf{i}}\left|\vec{v}(\vec{\mu}(s_p,\vec{x}_{\mathbf{i}})) - (\vec{\mu}(s_{p+1},\vec{x}_{\mathbf{i}}) - \vec{\mu}(s_p,\vec{x}_{\mathbf{i}}))\right|^2. \quad (14)$$

For motion sub-iterations, we use the original deformation-based OFC (3), as the motion parameters need to be estimated using the entire cycle.

IV. Method of Alternating Minimization with respect to Volume and Velocity

The total cost functional in (7) is nonlinear, nonconvex, and ill-conditioned. To avoid undesirable local minima, we use the same method of alternating minimization with dynamic parameter updates that we introduced in the previous work [9].

To briefly explain the method, each global iteration consists of a set of volume sub-iterations and a set of motion sub-iterations. The cost functional is minimized with respect to either $\mathbf{f}$, or $\mathbf{u}$ and $\bar{\mathbf{s}}$ in an alternating fashion, while keeping the other variable(s) fixed.

Starting volume sub-iterations with a large λ when all motion parameters are initialized as zero ends up underestimating the motion. On the other hand, a small λ will cause false motion detection due to the sparse angle artifacts. We use dynamically changing λ and δ to address both effects: motion underestimation and false motion.

In our approach, the value of λ oscillates throughout the global iterations. With an oscillating λ, global iterations have another chance to catch small motions that could have been lost in previous iterations, which the static parameter setting cannot achieve. Also, we select δ to be large initially, and then gradually decrease its value as the global iterations progress. This approach initially identifies large features and ignores minor details in phase volumes to estimate global motion. In later iterations, the algorithm adds more details to phase volumes and estimates local motion.

V. Test Results

We present reconstruction results for one simulated and one clinical dataset. The former was generated and latter was acquired using Varian TrueBeam treatment device [10] with half-fan beam geometry. For the simulated dataset, we use a synthetic, sinusoidal in time motion.

The amplitude of the simulated motion is maximum at a point inside the patient, and goes to zero in a radial fashion away from the maximum following the Gaussian curve. The maximum peak-to-peak amplitudes of the motion in the y and z directions are 15 voxels (i.e., 18.75 mm), while there is no motion in the x direction. We also assume the half-fan beam geometry of the Varian TrueBeam treatment device.

For the clinical dataset, chest motion amplitude was recorded using TrueBeam's respiratory gating system and then converted to the breathing phase.

Fig. 1 shows the transverse slices of the reconstructed object of the simulated dataset using our proposed algorithm (the top row), the ground truth images (the middle row), and the difference between the reconstruction results and the ground truth (the bottom row). The reconstruction results of the body are nearly identical with the ground truth.

Fig. 2 shows the comparison of the transverse slices between the existing clinical reconstruction software *Advanced 4D* [8] of the TrueBeam treatment device (two left images 2(a)–(b)) and our proposed reconstruction algorithm (two right images 2(c)–(d)) obtained using the same clinical dataset (the results for two additional clinical cases as well as comparisons with our previous method [9] will be shown at the conference). By comparing 2(a)–(b) with 2(c)–(d), one can observe that the proposed algorithm significantly reduces the streak artifacts, allowing for performing more focused on-the-target treatment of patients.

VI. Conclusions

We developed a robust motion estimation and compensation algorithm for 4D CBCT. The algorithm uses the cyclic motion model incorporated into the OFC. The experimental results show that the use of a cyclic motion model significantly reduces sparse-view streaks and false motion artifacts.

For the simulated data, we are able to get the reconstructed phase volumes that are nearly error-free.

The reconstruction results from the clinical data demonstrate that presented in this paper algorithm can significantly reduce artifacts and improve image quality compared to imaging results of clinical reconstructions.

References

[1] J.-J. Sonke, L. Zijp, P. Remeijer, and M. van Herk, "Respiratory correlated cone beam CT," *Medical physics*, vol. 32, no. 4, pp. 1176–1186, 2005.

[2] T. Li, A. Koong, and L. Xing, "Enhanced 4D cone-beam CT with inter-phase motion model," *Medical physics*, vol. 34, no. 9, pp. 3688–3695, 2007.

[3] Q. Zhang, Y.-C. Hu, F. Liu, K. Goodman, K. E. Rosenzweig, and G. S. Mageras, "Correction of motion artifacts in cone-beam CT using a patient-specific respiratory motion model," *Medical physics*, vol. 37, no. 6Part1, pp. 2901–2909, 2010.

[4] Z. Qi and G. Chen, "Performance studies of four-dimensional cone beam computed tomography," *Physics in Medicine and Biology*, vol. 56, pp. 6709–6721, 2011.

[5] M. Brehm, P. Paysan, M. Oelhafen, and M. Kachelrieß, "Artifact-resistant motion estimation with a patient-specific artifact model for motion-compensated cone-beam CT," *Med. Phys.*, vol. 40, no. 10, pp. 1–13, 2013.

[6] C. M. Rank, T. Heußer, M. T. Buzan, A. Wetscherek, M. T. Freitag, J. Dinkel, and M. Kachelrieß, "4D respiratory motion-compensated image reconstruction of free-breathing radial MR data with very high undersampling," *Magn. Reson. Med.*, vol. 77, no. 3, pp. 1170–1183, 2017.

[7] H. Zhang, J. Ma, Z. Bian, D. Zeng, Q. Feng, and W. Chen, "High quality 4D cone-beam CT reconstruction using motion-compensated total variation regularization," *Phys. Med. Biol.*, vol. 62, pp. 3313–3329, 2017.

[8] J. Star-Lack, M. Sun, M. Oelhafen, T. Berkus, J. Pavkovich, M. Brehm, M. Arheit, P. Paysan, A. Wang, P. Munro, D. Seghers, L. Carvalho, and W. Verbakel, "A modified McKinnon-Bates (MKB) algorithm for improved 4D cone-beam computed tomography (CBCT) of the lung," *Med. Phys.*, vol. 45, no. 8, pp. 3783–3799, 2018.

[9] S. Yoon, A. Katsevich, M. Frenkel, P. Munro, P. Paysan, D. Seghers, and A. Strzelecki, "A motion estimation and compensation algorithm for 4D CBCT of the abdomen," *15th Int. Meet. Fully Three-Dimensional Image Reconstr. Radiol. Nucl. Med.*, vol. 11072, no. May, p. 83, 2019.

[10] S. Lang, M. Zamburlini, A. Stüssi, J. Hrbacek, and S. Klöck, "Ep-1298: Evaluation of dosimetric and geometric stability of a new digital linear accelerator over a period of 3 years," *Radiotherapy and Oncology*, vol. 106, p. S490, 2013.

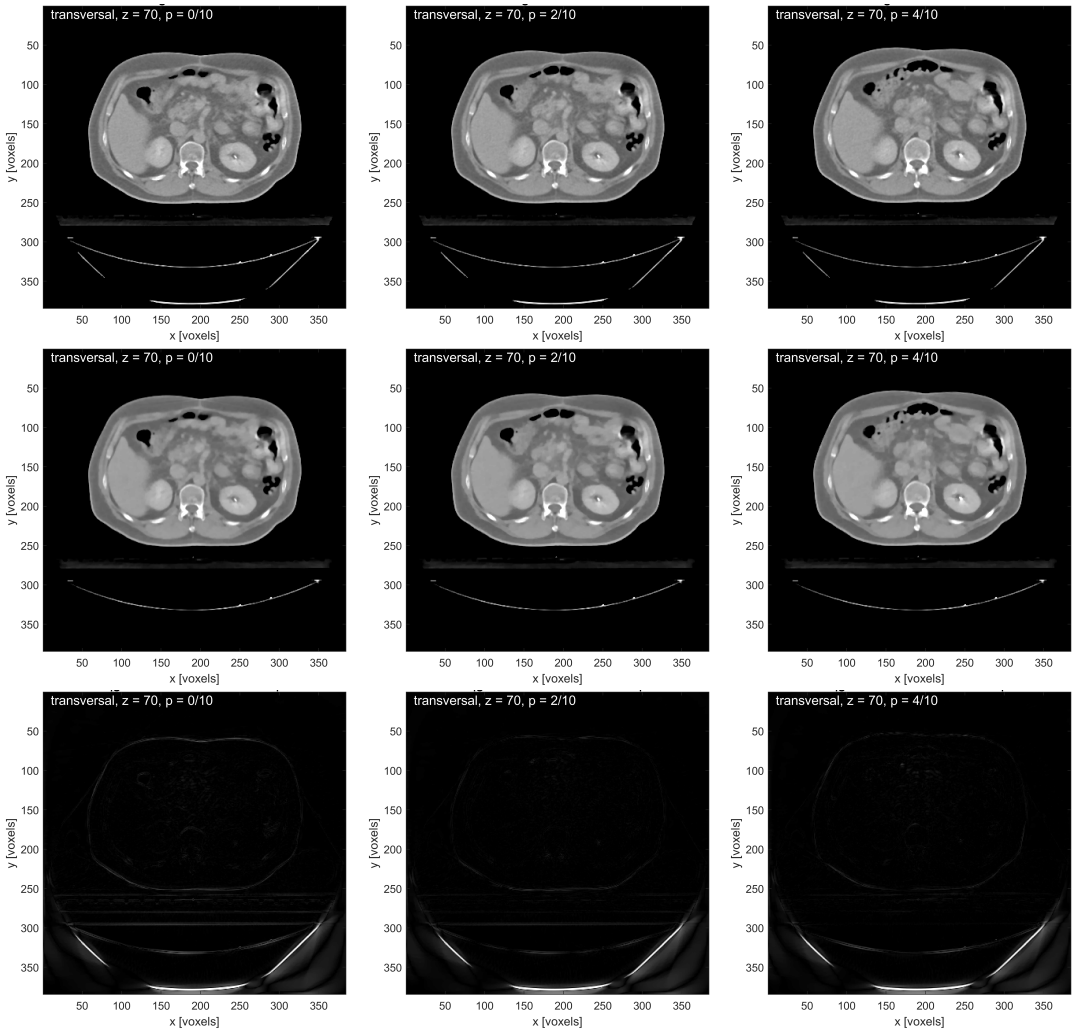

Fig. 1: Transverse slice of the volume $f_{p,\mathbf{i}}$ reconstructed from a simulated dataset based on sinusoidal discrete motion. First half of the breathing cycle is shown. From left to right: p/N_p = 0/10 (left), 2/10 (middle), and 4/10 (right). From top to bottom: ground truth (top), reconstruction (middle), and the difference $|\text{ground truth} - \text{reconstruction}|$ (bottom). WL = 0.22, WW = 0.16 for the top and middle row images. WL = 0.075, WW = 0.075 for the bottom row images.

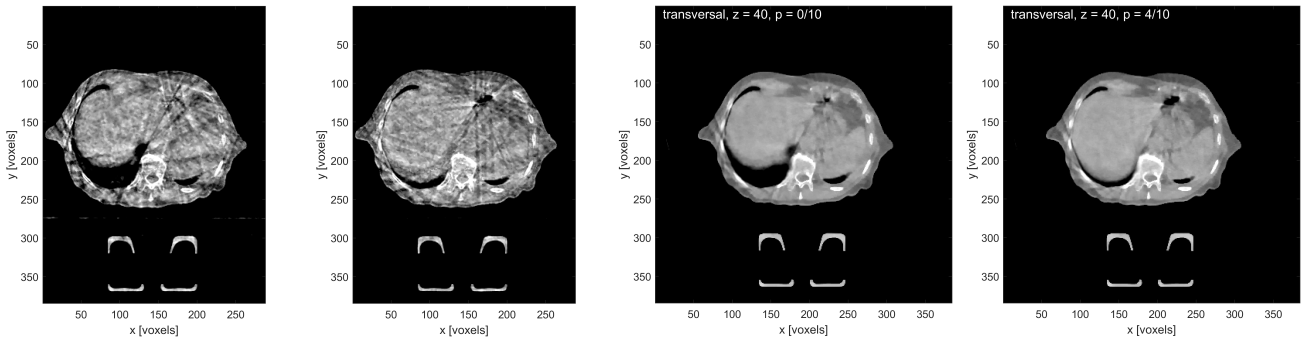

(a) (b) (c) (d)

Fig. 2: (a)–(b) Transverse slice of the existing clinical reconstruction result (Advanced 4D) at p/N_p = 0/10 and 4/10, respectively. (c)–(d) Corresponding transverse slice of the reconstruction result with the proposed algorithm at p/N_p = 0/10 and 4/10, respectively. WL = 0.22, WW = 0.16 for all images.